Flows over backward-facing steps with different spanwise widths

Ke Zheng,* Heri Setiawan,† Jimmy Philip, Junghoon Lee,‡ and Jason P. Monty§
Department of Mechanical Engineering, University of Melbourne, Parkville, Victoria 3010, Australia

(Received 6 August 2024; accepted 5 November 2024; published 4 December 2024)

The separated and reattached flow over backward-facing steps with different spanwise widths is experimentally investigated in a wind tunnel. The height and streamwise length of steps are fixed at 19 mm and 3.95 m, respectively. Five different spanwise aspect ratios (AR), defined as the ratio of step width to height, 1, 2, 4, 8, and 16, are tested. The Reynolds number based on the step height and free-stream velocity is 11 300, and a well-developed turbulent boundary layer is present before the flow encounters the step. Planar particle image velocimetry is employed to measure the velocity field along the centerline over and behind the steps. Results show that the three-dimensional effect becomes more significant as AR increases up to 4 and persists when AR = 8, likely attributed to the corner vortices formed alongside the step, as well as rolled up the sidewall shear layer. Surface oil-film flow visualization shows that the effect of side edges on the central flow remains significant until AR reaches 16. For AR = 16, the step flow is nominally two dimensional and exhibits similar characteristics as a typical two-dimensional backward-facing step flow. The mean reattachment length increases with AR and then tends to approach an asymptotic level, while a much larger AR may be required for the saturation in the span of the reattachment zone. For AR = 4 and 8, a distinct flow structure is observed, characterized by jettisoned flow away from the floor after reattachment, and the distributions of Reynolds stresses are therefore not confined within a narrow region below the step height. The highest Reynolds stresses are observed when AR = 4 while the largest-scale turbulence appears when AR = 2. Furthermore, as AR increases, the evolution of vortical structures becomes more complex and the spreading of the shear layer slows down.

DOI: 10.1103/PhysRevFluids.9.124601

I. INTRODUCTION

Separated flows are widely found in diverse engineering applications, such as behind ships, airfoils, buildings, turbine blades, and inside pipes or combustors. The flow separation is usually induced by an adverse pressure gradient or sudden changes in geometry. The inherent instability of separated flow promotes the flow complexity and can lead to detrimental effects. Understanding the characteristics of separated flow is necessary to control the flow separation and thus has considerable engineering significance. The backward-facing step (BFS), as sketched in Fig. 1(a), has been commonly used as a prototype to study the separated and reattached flow owing to its simple geometry [1]. Although the complexity of BFS flow has been summarized by Roos and

*Contact author: kzheng1@student.unimelb.edu.au
†Present address: Ocean Engineering Program, Institut Teknologi Bandung, Bandung, Jawa Barat 40132, Indonesia.
‡Present address: Platforms Division, Defence Science and Technology Group, Victoria 3207, Australia.
§Contact author: montyjp@unimelb.edu.au

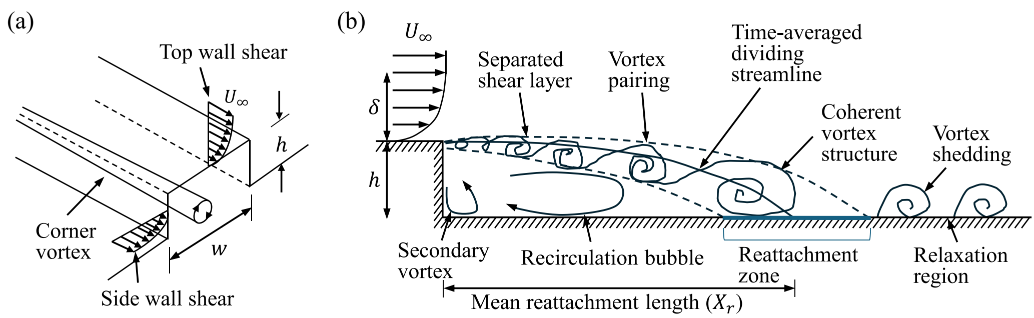

FIG. 1. (a) An oblique view of a backward-facing step, with the corner vortex tube illustrated on one side (not to scale). (b) Typical flow structures of the backward-facing step flow.

Kegelman [2], the instability of the separated flow and the development of vortical structures have not been fully understood so far. Over the past several decades, considerable studies have been carried out on BFS flow, typically using a two-dimensional (2D) planar BFS configuration with a large spanwise aspect ratio (AR), defined as the ratio of step spanwise width (w) to its height (h), i.e., AR $\equiv w/h$ [3–5]. Several researchers also employed axisymmetric BFS geometry, such as in suddenly expanding pipes [6] or concentric cylinders [7], to minimize the three-dimensional (3D) effects, while few studies on BFS flow with a consideration of 3D effects could be found. The planar BFS models ever used span the entire channel width, i.e., both sides of the step are bounded by the channel sidewalls, forming internal corners (concave). These models are suited for studying flow separation and reattachment inside a diffuser or combustor. However, a BFS with external corners (convex), which is more representative of the flow over a ship's superstructure or buildings, has rarely been studied. As illustrated on one side of the step in Fig. 1(a) (not to scale), a vortex tube forms along the external corner, with its size growing as it develops [8], but its influence on the flow behind a step remains unclear. This study presents planar particle image velocimetry (PIV) measurements of the flow over 3D and 2D BFSs. Of particular interest is the external corner effect on the flow features as the step width varies, which is significant for the design of ship superstructure, buildings, trains, etc.

The 2D BFS flow has been extensively investigated. Early researches were conducted by flow visualization techniques, hot-wire, pressure probe, and laser Doppler velocimetry (LDV) methods to study the mean flow features qualitatively and quantitatively [3,9–11]. Recently, with the development of the PIV technique, the flow properties within the separation bubble and the shear layer have been further studied [4,12,13]. Meanwhile, numerical methods, such as direct numerical simulation (DNS) [14,15], large eddy simulation (LES) [16], and detached eddy simulation (DES)-like approaches [17], have been applied to study the flow over 2D or 3D BFSs. The achievements have been gradually reviewed in the literature [1,18,19].

Figure 1(b) shows the sketch of detailed flow characteristics behind a typical BFS. The BFS flow consists of main features of separated and reattached flow, which are the recirculation bubble, the free shear layer, the reattachment zone, and the relaxation region [5,10]. Similar mean flow structures within the recirculation region have been reported in numerous studies [20–22]. The primary clockwise-rotating vortex extends from the step to the reattachment point, while a secondary counter-rotating vortex, induced by backflow separated from the bottom surface, remains in the corner of the step, forming a comparatively quiet region [23]. This phenomenon is observed not only behind a 2D planar BFS, but also behind an axisymmetric BFS [6] and BFSs with small AR [14]. Troutt *et al.* [24] investigated the separated shear layer of a BFS flow and found that the free shear layer emanating from the step edge grows initially similarly to a planar mixing layer [25]. Vortices within the shear layer form by rolling up due to Kelvin-Helmholtz (KH) instability and grow by pairing, leading to the growth of shear layer thickness. The mechanisms of vortex rolling up and pairing are described in detail by Winant and Browand [26]. Due to the existence of the separation bubble, the free shear layer behind the BFS curves down and impinges on the bottom wall. Vortical structures in the shear layer keep growing through amalgamation until they approach the reattachment zone. This pairing process undoubtedly contributes to high turbulence intensity and Reynolds shear stress [5]. Troutt *et al.* [24] also suggested that the final coherent vortex structures have a length scale of at most one step height, later supported by Hu *et al.* [17]. These final vortical structures shed after reaching their maximum size [27], leading to a rapid decay in Reynolds stresses. As a consequence, the shear layer was found to continue spreading downstream after reattachment into a redeveloping layer [3,10]. The mean streamwise velocity profiles measured by Bradshaw and Wong [10] showed that the flow did not fully recover even at more than 50 step heights behind the step, indicating the remarkable persistence of large-scale vortices. Moreover, due to the unsteady motions of the vortical structures, two low-frequency characteristics, which are the flapping of the shear layer and the oscillation of the reattachment point within the reattachment zone, have been observed by many researchers [11,13,14,18,28].

The mean reattachment length (X_r) has been identified as the primary parameter to study the BFS wake characteristics in earlier literature. Reattachment is defined as the locus of points where the limiting streamline of the time-averaged flow rejoins the surface [29]. The effects of inflow conditions and geometry parameters on the reattachment length have been well reviewed by Eaton and Johnston [18] and Hu *et al.* [19]. They identified important parameters, including the Reynolds number (Re), free-stream turbulence intensity, boundary layer state and boundary layer thickness at separation, expansion ratio (ER = channel height/(channel height − step height), and AR. The effect of Re was of the most interest. Armaly *et al.* [30] found that the mean reattachment length increases rapidly with Re when the flow is laminar, but decreases with Re in the transitional regime, and increases again with Re for turbulent flow. When the flow is fully turbulent, the mean reattachment length reaches an asymptotic value, varying from 4.2 to 8.6 step height in the literature, depending on geometry and inflow conditions [18]. The Re independence for sufficiently high Reynolds number was also observed by Durst and Tropea [11], Adams and Johnston [31], and Nadge and Govardhan [12] when they studied the effect of both Re and other parameters. When the incoming flow is fully developed turbulent flow, it was also found that the effect of boundary layer state and thickness at separation has a minimal effect on the reattachment length [31]. As a crucial parameter for the design of BFS with internal corners, the effect of ER has been systematically studied. It was found that the reattachment length increases linearly with ER before reaching a nearly constant value when ER ≈ 1.8 [11,12]. However, the effect of AR has only been studied by de Brederode and Bradshaw [32] on the two-dimensionality of BFS flow using oil-film visualization. They reported that the mean reattachment length decreases with increasing AR and the effect of AR is minimized when AR $\geqslant 10$, where the flow in the central plane becomes quasi-2D. They also observed that, for AR < 10, the reattachment length appears to vary differently with the boundary layer state at separation compared to larger AR, probably due to the channel sidewalls. The 3D effect of the internal corners formed by the step and channel sidewalls on the BFS flow was also presented by Shih and Ho [23] with an AR of 3. They observed strong spanwise movement and reported a wavy distribution of reattachment points along the spanwise direction. Although the detailed mechanism through which the flow in the corner region affects the wake is not clear, the 3D effect undoubtedly plays an important role in the wake behind a BFS with a small AR. Therefore, for a BFS with external corners, i.e., without sidewalls, further investigation is in demand to understand the effect of external corners, as well as the effect of AR, on the flow dynamics.

In this paper, we investigate in a systematic manner the flow over a BFS with different spanwise widths (AR = 1, 2, 4, 8, and 16). In Sec. II, the experimental setup used to measure the central streamwise-vertical flow field is presented. In Sec. III, the experimental data are analyzed and discussed in terms of mean flow structures, flow conditions prior to the step, reattachment length, turbulence statistics, and vortical structures within the shear layer. The primary aim is to study the effect of AR on the BFS flow characteristics. Despite extensive research on BFS flows, very few studies address the AR effect, and no existing studies have employed a BFS configuration similar

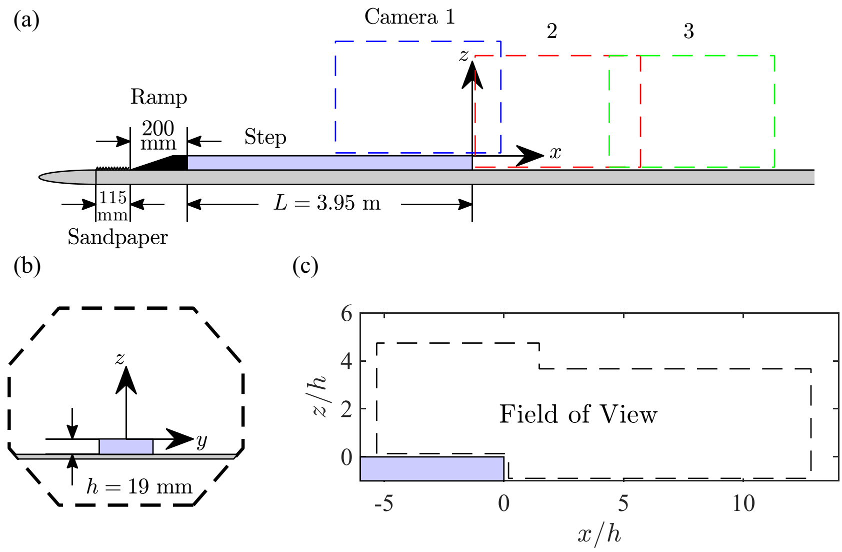

FIG. 2. Schematic of test section (not to scale) in (a) side view and (b) rear view. (c) Stitched field of view.

to this study, where a well-developed turbulent boundary layer encounters the step, limiting direct comparisons with existing literature. Where applicable, comparisons will be made with relevant studies on bluff bodies. Finally, a summary of major findings in this research is provided in Sec. IV, along with a discussion on the limitation of this study and recommendations for future work.

II. EXPERIMENTAL SETUP

The experiments were conducted in a closed-circuit wind tunnel in the Walter Bassett Aerodynamics Laboratory at the University of Melbourne. The operating section in the wind tunnel is 6 m long with a hexagonal cross section, which has dimensions 1.28 m $\times$ 1.74 m (height $\times$ width). The blockage effect is minimized due to the slotted sidewalls. A flat plate, representing the floor, is embedded inside the tunnel with a smooth elliptical leading edge.

Figures 2(a) and 2(b) show the schematic of the test section in side view and rear view, respectively. The BFS is formed by a strip or plate made of plywood mounted along the longitudinal direction in the middle of the wind tunnel. The midpoint in the span at the top of the step edge is defined as the origin of the adopted coordinate system, with the streamwise, spanwise, and vertical directions defined as x, y, and z axes, respectively. A sandpaper sheet with grade P40 and a length of 115 mm was installed before the step model as a flow tripping device in order to generate a thick turbulent boundary layer. A 7° slope ramp of 200 mm was attached to the model leading edge to avoid flow separation. In order to investigate the effect of AR, step models with constant height, $h = 19$ mm, constant length, $L = 3.95$ m, and five different spanwise widths, w, corresponding to AR $\equiv w/h = 1, 2, 4, 8$, and 16, were tested. The free-stream velocity (U_∞) was maintained at 9.5 m/s and the kinematic viscosity of air (ν) is 1.6×10^{-5} m^2/s evaluated based on room temperature at 20 °C. Therefore, the Reynolds number based on the free-stream velocity and step height ($\mathrm{Re}_h = U_\infty h/\nu$) is 11 300.

Planar PIV was employed to measure the velocity field in the x-z plane at the centerline for each BFS model. Rosco fog theatrical droplets with a diameter of 1–2 μm were injected as seeding particles to trace the airflow. The Innolas Spitlight Compact Nd:YAG double pulse laser was used to generate a laser sheet with a thickness of 1 mm. The pulse energy is 130 mJ at a wavelength of 532 nm. Three 14-bit PCO4000 cameras with a resolution of 4008 pixels $\times$ 2672 pixels, equipped with 180-mm Tamron optical lenses, were used to record image pairs of the illuminated flow field at an acquisition rate of 1 Hz. The individual field of view has dimensions of 132 mm × 88 mm and spatial resolution of 33.3 μm/pixel. The stitched field of view, shown in Fig. 2(c), has a height of 4.6h and starts from 5.2h upstream of the step to 12.8h downstream of the step. The three camera fields of view are indicated in Fig. 2(c) in different colors. For each case, 1815 pairs of images were taken for data convergence. The PIV image pairs were processed with an in-house code by cross-correlating the particle patterns in small interrogation windows to obtain instantaneous velocity fields (details and validation can be found in Refs. [33,34]). The interrogation window size reduces from 64 pixels × 64 pixels at the initial pass to 24 pixels × 24 pixels at the final pass, both at 50% overlap, leading to a spacing of 0.4 mm between velocity vectors in both streamwise and vertical directions. Following Adrian and Westerweel [35], the uncertainty in detecting the displacement correlation peak is typically 0.1–0.2 pixels. Thus, with time intervals between PIV images of 70 μs and the image resolution of 33.3 μm/pixel, the uncertainty in the velocity estimation is 0.048–0.095 m/s ($\leqslant$1% of U_∞).

Additionally, surface oil-film flow visualization was carried out to further investigate the flow along the spanwise direction using a mixture of kerosene, aluminum powder, and oleic acid. The kerosene is a typical light oil used for surface oil flow visualization carrying the pigment, which in this study is the white aluminum powder. To control the clumping of the aluminum powder, the oleic acid was used as an additive [36]. The best recipe was found using a trial and error method. The oil mixture was applied to the step top surface from 5h upstream of the step edge and to the region of interest behind the step, which extends to 12h downstream of the step. All painted regions were covered by a thin black vinyl sheet so that the streaky deposit of the white aluminum powder could be clearly seen. Time-lapse photographs were taken with a GoPro camera mounted at the ceiling of the wind tunnel.

In this paper, by applying the Reynolds decomposition, the instantaneous velocity can be decomposed into time-averaged and fluctuation components, denoted by $\overline{(\cdot)}$ and $(\cdot)'$, respectively. For brevity, capital U and W are used to denote the mean velocities, and the notation AR16 is used to denote the step with AR of 16 and so on for all other cases.

III. RESULTS AND DISCUSSION

A. Mean flow structures

Figure 3(a) shows the contours of streamwise mean velocity (U) for all the cases examined. The mean flow separates at the step edge and reattaches to the bottom wall at a distance downstream of the step. A recirculation region is formed just behind the step, with different sizes according to AR. The maximum speed of the reverse flow within this region initially increases with AR, peaking at AR4, then decreases with increasing AR. Its magnitude is around 20% U_∞ in the AR1, AR2, and AR8 cases, similar to the observation behind a 2D BFS [18], and it reaches 25% U_∞ in the AR4 case while it is only 15% U_∞ when AR = 16. The white dashed line represents the $U = 0$ contour, and its intersection with the bottom wall defines the mean reattachment point of the separated shear layer, which moves farther away from the step as AR increases. The shift with AR of the downward flow region (in blue) in the wall-normal mean velocity (W) contours, shown in Fig. 3(b), also confirms that the flow reattaches at a farther downstream location as AR increases. Moreover, there is an interesting observation in the AR4 and AR8 cases, where the flow after reattachment appears to eject upward from the floor rather than impinge onto it as seen in the other cases.

The streamlines of U and W in Fig. 4 further illustrate that the flow structures vary significantly with AR. The green dash-dotted line indicates the line of $U = 0$, separating the forward and backward flow. Recirculation bubbles could be clearly seen in the AR1, AR2, and AR16 cases, while a distinctly different flow pattern is observed in the AR4 and AR8 cases, where the flow after reattachment is jettisoned away from the bottom wall. The isopleth of $\psi(z) = \int_{\mathrm{wall}}^{z} U dZ = 0$ (red solid line), which marks zero net streamwise mass flow flux below this height, is defined

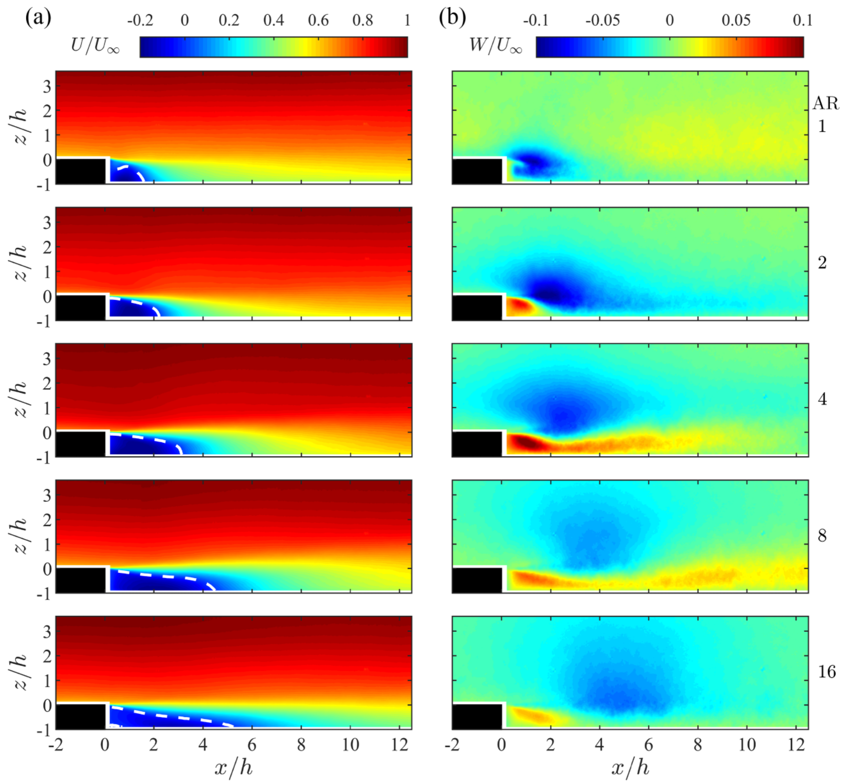

FIG. 3. (a) Contours of streamwise mean velocity (U). The white dashed line represents the line of $U = 0$. (b) Contours of wall-normal mean velocity (W).

as the dividing or separating streamline [12]. It, together with the step leeward face and the bottom wall, bounds the recirculation region. The streamwise extent of the separation bubble grows monotonically as AR increases, while in the wall-normal direction, the separation bubble is confined below the step height only when AR = 16. In the AR16 case, a secondary separation bubble forms

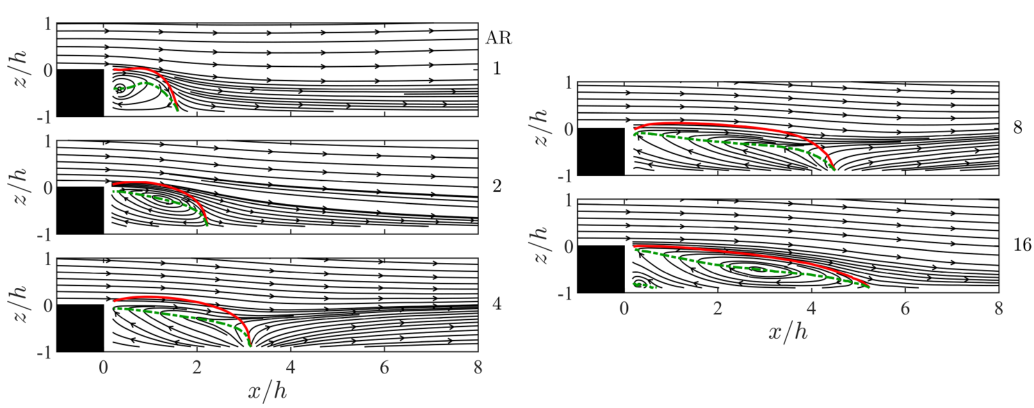

FIG. 4. Mean streamlines of U and W. The green dash-dotted line represents the line of $U = 0$. The red solid isopleth is $\psi(z) = \int_{\mathrm{wall}}^{z} U dZ = 0$, representing the upper boundary of the primary separation region (not shown for the secondary vortex in the AR16 case).

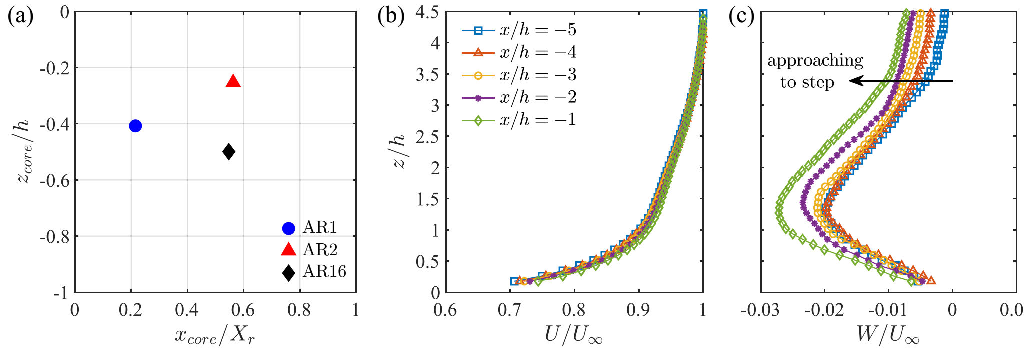

FIG. 5. (a) The vortex core locations of the mean separation bubble in the AR1, AR2, and AR16 cases. [(b) and (c)] Flow development before the step in the AR4 case at upstream locations $x/h = -5, -4, -3, -2$ and -1 (U and W).

at the corner, similar to observations behind a BFS with internal corners with AR varying from 4 to infinity [6,12,14]. However, the streamwise size of the corner bubble in this study is only 13% of the primary bubble, significantly smaller than the 20–28% reported for those BFSs with internal corners. The boundary ($\psi = 0$) of the secondary bubble is not shown in the figure as the limited field of view may lead to an inaccurate estimation of its location. Although no secondary separation bubble presents in the other cases, it cannot be fully determined that a corner bubble with a much smaller size does not exist, as the region very close to the corner was not fully captured. Nonetheless, it can be concluded that the 3D flow induced by the external corner, as opposed to the internal corner flow, may result in a reduced dimension of the secondary recirculation region, supporting the speculation by Tinney and Ukeiley [37].

The vortex core of the mean separation bubble is also used to characterize the recirculation zone, which can be estimated as the intersection point of the $U = 0$ and $W = 0$ lines [12]. However, in the AR4 and AR8 cases, these two lines approach each other closely but do not intersect, indicating the absence of a distinct vortex core. For the other three cases, the normalized locations of the vortex core ($x_{\rm core}/X_r$, $z_{\rm core}/h$) are shown in Fig. 5(a). Note that the parameter X_r represents the mean reattachment length and will be discussed in detail in Sec. III C. In the AR16 case (black diamond), the vortex core is located near the midpoint of the recirculation region. In contrast, the vortex core in the AR1 case (blue circle) lies above the midpoint and very close to the step leeward face, while in the AR2 case (red triangle), it is located even higher than in the other two cases. This upward shift of the vortex core in the AR1 and AR2 cases may be attributed to relatively stronger upward flow behind the step, suggesting a transition towards the jettisoned flow pattern observed in the AR4 and AR8 cases.

A similar jettisoned flow structure was reported by Tinney and Ukeiley [37] behind the first step of a 3D double BFS, which has a short streamwise length, a step height of 12.7 mm, and a spanwise AR of 3. They suggested the formation of an arch-shaped vortex behind the step, as those found in the wake of cubes or bluff bodies with AR ranging from 1 to 8 [38,39], and ascribed the ejection of fluid away from the surface to the counter-rotating vortex pair shed from this arch-shaped vortex. Additionally, Kim *et al.* [40] observed some upward flow behind a 3D rectangular prism in an off-center flow field, which might be attributed to the development of a horseshoe vortex along the sidewalls. However, in the present study, the absence of a vortex core in the midspan implies no arch-shaped vortex forms in the AR4 and AR8 cases, and the significantly long streamwise extent of the step prevents the formation of a horseshoe vortex wrapping around it from upstream. Instead, the flow separation from the sidewalls and induced side vortices may similarly contribute to the upward flow. Meanwhile, the external corner vortices that develop alongside the extended step (illustrated on one side in Fig. 1(a) but not to scale) could be significant, as suggested by Moinuddin *et al.* [8].

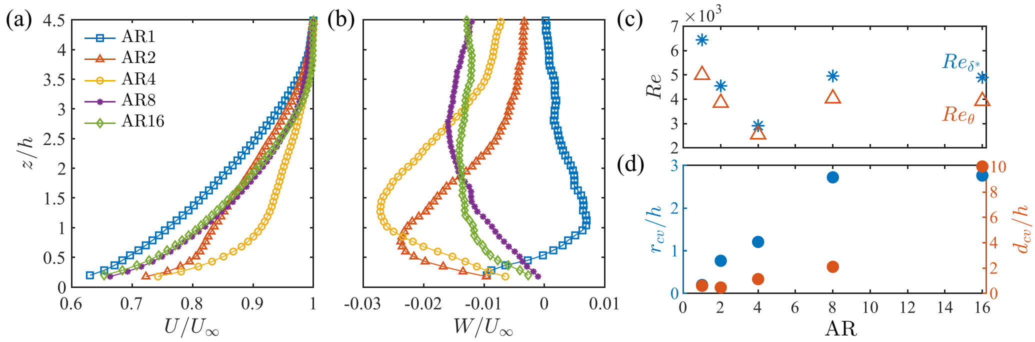

FIG. 6. [(a) and (b)] Comparison in velocity profiles (U and W) prior to the step (at $x/h = -1.0$). (c) Reynolds numbers prior to the step edge (at $x/h = -1.0$). (d) Estimated radius of influence of the corner vortices (r_{cv}) and the space in between (d_{cv}).

These corner vortices are generated due to the pressure difference between the side and top surfaces and persist downstream of the step while being deflected subtly toward the center, as demonstrated by Tinney and Ukeiley [37] in multiple cross planes. Their scale and spacing may vary with the step width, affecting the wake to different degrees. In the AR4 and AR8 scenarios, large-scale corner vortices in close proximity may form and interact with the separated flow, leading to the observed jettisoned flow feature. A conjecture regarding their size and spacing with varying AR will be provided in the following section; however, further investigations are required to understand the detailed structures and their interaction with the separated flow.

B. Flow conditions prior to separation

To investigate the AR effect on the BFS flow, the vertical profiles prior to the step edge are first examined. The flow development upstream of the step is similar for each individual case. Figures 5(b) and 5(c) show the vertical profiles of mean streamwise (U) and vertical (W) velocities at five upstream locations in the AR4 case as an example. The U profiles far above the step collapse well, while the magnitude of U near the step top surface slightly increases as it approaches the step edge. Compared to U, the variation in W with streamwise distance is more noticeable, where W becomes negatively larger as it moves to the step edge. The increase in U and the decrease in W with x in the AR1 and AR2 cases are smaller compared to AR4, but such changes in the AR8 and AR16 cases are comparable to AR4. This can be ascribed to the development of the corner vortices with various scales and spacing alongside the step.

The comparison across all cases just prior to separation clearly reveals how the impact of corner vortices varies with AR. In Fig. 6(a), the streamwise velocity deficit is the largest in the AR1 case. It gets smaller as AR increases to 4 and gets larger again when AR = 8, while the U profile for AR16 is comparable to that of AR8. This variation with AR is also reflected in the boundary layer properties listed in Table I, which includes the 95% boundary layer thickness (δ_{95}), displacement thickness (δ^*), momentum thickness (θ), and associated Reynolds numbers. Figure 6(c) displays the variation of Re_{δ^*} and Re_θ with AR. This suggests that the corner vortices with the incoming flow have a direct effect on the streamline patterns observed for different ARs.

The impact of the corner vortices is further illustrated by the wall-normal velocity profiles in Fig. 6(b). For AR1, the narrow step width enhances the interaction of surrounding flows and prevents the formation of large-scale corner vortices. Thus, the flow direction is affected only to a limited height above the step. As the spanwise width increases, larger-scale counter-rotating vortices form above the step and their interaction drives the central flow downward. As a result, in the AR2 and AR4 cases, the W profiles form a noticeable wavy distribution. The peak of W becomes negatively larger and occurs higher above the step with larger AR, indicating the growth of corner vortex size.

TABLE I. Boundary layer properties just upstream of the step edge (at $x = -1.0h$). Air properties are evaluated at 20 °C and 1 atm.

AR	h (mm)	δ_{95} (mm)	δ^* (mm)	θ (mm)	U_∞ (m/s)	Re_h	$\mathrm{Re}_{\delta_{95}}$	Re_{δ^*}	Re_θ
1	19	59.3	11.1	8.6	9.3	11 010	34 380	6440	5000
2	19	54.9	7.8	6.6	9.3	11 030	31 870	4550	3850
4	19	39.3	5.0	4.4	9.3	11 100	22 960	2910	2550
8	19	49.7	8.3	6.8	9.5	11 300	29 570	4960	4030
16	19	49.3	8.3	6.6	9.5	11 240	29 160	4900	3930

However, in the AR8 case, the wavy pattern of W is less significant, suggesting that the vortex scale may reach a maximum at some AR between 4 and 8, possibly constrained by the step height.

Although the exact dimensions, shapes, and locations of the corner vortices remain unknown, the extent of their influence could be inferred from the location of the most negative W. Figure 6(d) presents the estimated radius of influenced regions (r_{cv}) and the spacing between them (d_{cv}), which together determine the effect of corner vortices on the midspan flow. The limited data points suggest that r_{cv} increases with AR until it reaches $2.7h$ when AR $= 8$, after which d_{cv} becomes larger. As mentioned above, the vortex size may reach its maximum before AR $= 8$. Beyond that AR, while the radius of influence continues to expand with increasing AR, the strength of the effect in the midspan may diminish, resulting in a relatively uniform W profile for AR8. It is worth noting that, after separation, the corner vortices are deflected subtly towards the center due to the entrainment of the ambient flow from all open sides, leading to a wake structure similar to that observed for AR4 (see Fig. 4). In the AR16 case, the influence regions of the corner vortices are well separated, leading to a more uniform distribution of W.

For the nominally 2D case (AR16), Fig. 7 shows the turbulent boundary layer profiles at 50 mm upstream of the step edge ($x \approx -2.5h$). The friction velocity (U_τ) is estimated using the Clauser chart method as 0.37 m/s, giving a friction Reynolds number ($\mathrm{Re}_\tau = \delta U_\tau/\nu$) of 1515. The vertical profiles of mean streamwise velocity and Reynolds stress components, normalized by U_τ, show good agreement with the DNS wall boundary layer data with a similar friction Reynolds number ($\mathrm{Re}_\tau = 1561$) [41]. As the spatially under-resolved PIV measurement leads to some discrepancies in turbulence intensity, the missing energy in normal Reynolds stresses ($\overline{u'u'}^+$ and $\overline{w'w'}^+$) is calculated using an estimation tool developed by Lee *et al.* [42] based on the PIV spatial resolution ($\Delta x^+ = \Delta z^+ = 9.3$). By adding the estimated missing energy to the original PIV results (shown in green triangles), Figs. 7(b) and 7(c) show a closer match with the DNS data.

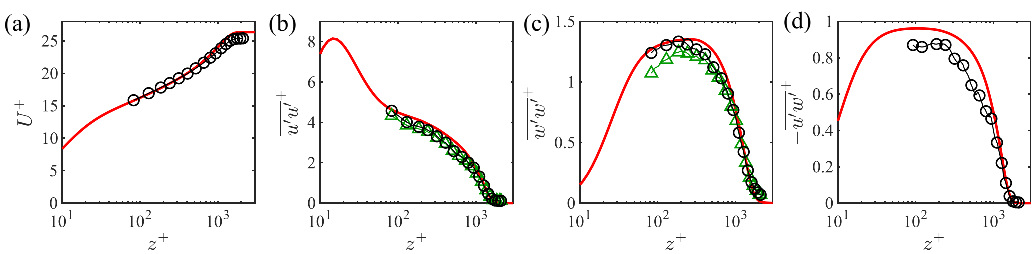

FIG. 7. Characterization of turbulent boundary layer at 50 mm upstream of the step edge ($x \approx -2.5h$) (open circles) compared to DNS data with similar friction Reynolds number (solid line). The vertical profile of normalized (a) mean streamwise velocity (U^+) and Reynolds stresses (b) $\overline{u'u'}^+$, (c) $\overline{w'w'}^+$, and (d) $-\overline{u'w'}^+$. Green triangles in (b) and (c) represent the original PIV results, while black circles include the estimated missing energy.

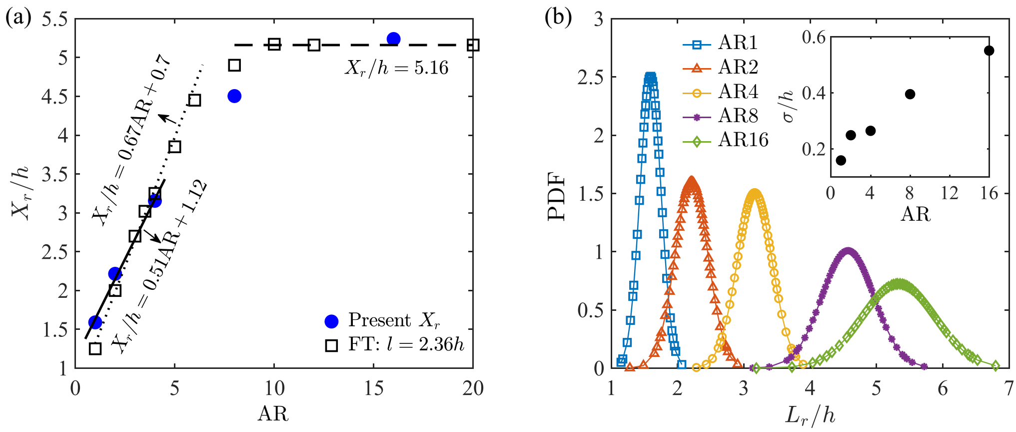

FIG. 8. (a) Variation of mean reattachment length (X_r) with AR. A linear equation (solid line) is fitted for AR $\leqslant 4$ using the least squares method. The empty square symbols plot the results of Fang and Tachie [39] and a linear function (dotted line) fitted for AR $\leqslant 6$. (b) Probability density function of intermittent reattachment length (L_r) and the inset shows the variation of standard deviation (σ) with AR.

C. Reattachment lengths

An essential parameter characterizing the BFS flow is the mean reattachment length (X_r), defined as the distance from the step leeward face to the mean reattachment location. There are four different methods used to determine the mean reattachment location. The most commonly used one is to determine from the mean flow field the point where the extrapolated line of $U = 0$ intersects with the bottom wall [30]. This point is typically estimated at the measurement locations closest to the wall. The second approach is to find the point where the wall shear stress is zero, but this can be hardly achieved in an experimental study. Third, the mean reattachment point could be estimated as where the mean separated streamline ($\psi = 0$) impinges on the wall [4]. This gives exactly the same result as the first method based on measurement data. The last one is the time fraction of forward flow (γ) approach proposed by Simpson [29] and is also widely used to determine the reattachment length [43,44]. Due to the instability of the separated flow, the instantaneous free shear layer does not impinge on the surface at a fixed point. As the flow upstream of the reattachment point is reverse and the flow downstream is forward, the mean reattachment point could be evaluated as the location of 50% forward flow fraction ($\gamma_{0.5}$). Le *et al.* [14] found that the first three methods give results within 0.1% of each other, while the fourth approach yields an $\approx$2% difference from the others as it considers only the flow directions. In this study, the $\gamma_{0.5}$ approach gives results with an average difference of 1.6% compared to the first method. Therefore, the mean reattachment location is determined by the point closest to the bottom wall where $U = 0$. However, the accuracy of X_r values is limited as the measurements do not cover the complete region extended to the floor.

Figure 8(a) shows the variation of X_r with AR and a linear line is fitted to the data for AR $\leqslant 4$ using the least squares method. Generally, X_r increases monotonically with relatively small AR, with a slope $d(X_r/h)/d\text{AR} = 0.51$, and then tends to approach a constant level for sufficiently large AR. This trend of increasing X_r is consistent with observations behind surfaced-mounted bluff bodies with finite streamwise extent by Martinuzzi and Tropea [38] and Fang and Tachie [39], using flow visualization and PIV techniques, respectively. However, this trend is contrary to the findings behind BFS flow with internal corners by de Brederode and Bradshaw [32]. This discrepancy can be attributed to the difference in the secondary flow structure between external and internal corner regions. The cross-flow around an external corner is driven away from it [45], allowing the expansion of the reattachment region as AR increases. Regardless of how X_r varies with relatively small AR, all studies reported that X_r approaches an asymptotic value when AR $\gtrsim 10$.

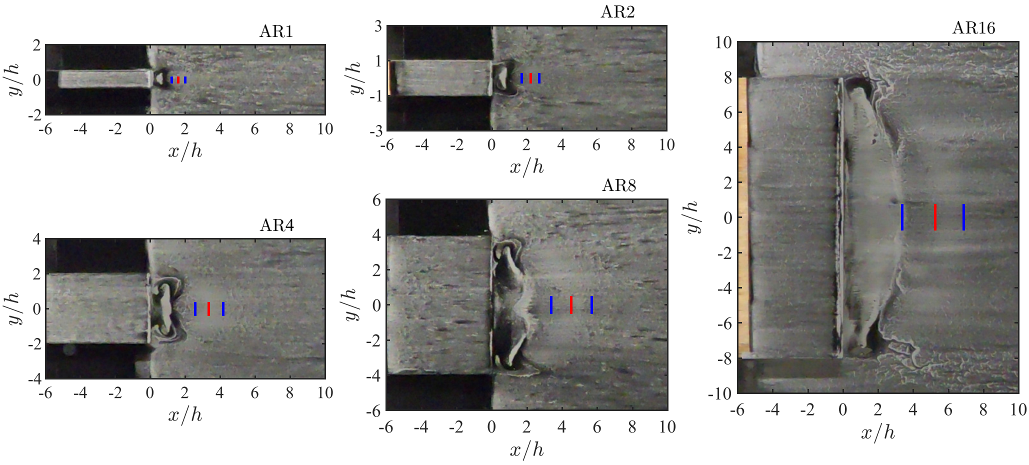

FIG. 9. Surface oil-film flow visualization. The middle red line indicates the mean reattachment location and the blue lines denote the ends of reattachment region in the midspan.

More specifically, experimental data from Fang and Tachie [39] behind bluff bodies with a body height of 30 mm and a length of 2.36 body heights are also plotted in Fig. 8(a). They found that X_r increases linearly when AR < 6 with a slightly larger slope of 0.67 and reaches a constant value of $X_r/h = 5.16$ when AR $\geqslant 10$ by studying 11 different AR cases ranging from 1 to 20. They clearly identified the 3D, transitional, and 2D regimes based on the relationship between X_r and AR. Although it cannot be exactly distinguished in this study due to insufficient data points, the rule observed by Fang and Tachie [39] can be applied without any contradiction. The X_r in the AR16 case, which is $5.24h$, is also comparable to their asymptotic value.

As aforementioned, the separated shear layer undergoes flapping motion, leading to oscillation of the reattachment point. Le *et al.* [14] reported a quasiperiodic movement of the reattachment location in their DNS study. They observed that the reattachment point moves downstream at a constant speed, corresponding to the growth of large-scale vortical structures, and then suddenly moves upstream, corresponding to the shedding of vortex from the separation bubble. This oscillation of the reattachment point may impose some challenges and thus need to be taken into consideration during practical design. The region where the free shear layer intermittently impinges is defined as the reattachment zone and can be quantitatively studied by the method of γ. The upstream and downstream ends of the reattachment zone can be estimated as the points where γ equals 5% and 95%, respectively [5,39]. The intermittent reattachment length, denoted as L_r, defines the distance from the step leeward face to the corresponding intermittent reattachment point. Figure 8(b) presents the probability density function (PDF) of L_r for all cases. As the separated shear layer develops farther downstream with larger AR, the vortical structures within the shear layer are more likely to have an elliptical shape with a larger scale in the streamwise direction. As a consequence, the span of the reattachment zone extends from $1h$ to $4h$ as AR increases. The standard deviation (σ) of the PDF, shown in the inset, almost increases linearly with AR. However, the shortest L_r values, indicated by the left ends of the PDF curves, for AR8 and AR16 are comparable. This suggests that, as AR increases, the saturation in the shortest L_r is reached first while a much larger AR is required for the saturation in the longest L_r.

Due to the flow separation from the side edges, the reattachment location varies along the spanwise direction, with the pattern altered by AR depending on how the induced secondary structures interact with the main flow. An overview of the side edge effects is presented by surface oil-film flow visualization in Fig. 9, where the mean reattachment location and the estimated ends of the reattachment region in the midspan are marked with red and blue lines, respectively. In the

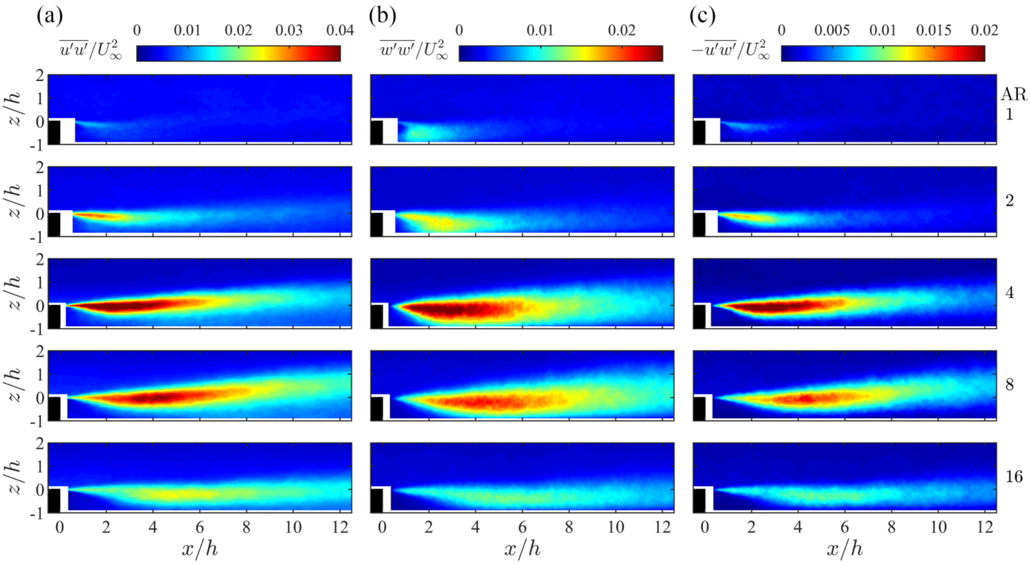

FIG. 10. Contours of Reynolds stress components: (a) streamwise Reynolds normal stress ($\overline{u'u'}$), (b) vertical Reynolds normal stress ($\overline{w'w'}$), and (c) Reynolds shear stress ($-\overline{u'w'}$).

AR1, AR2, and AR4 cases, overlapping of the side vortices is apparent. Although the side vortices are slightly separated for AR8, the interaction between them remains strong. In contrast, when AR = 16, the central flow appears nominally 2D, while the influence of side vortices persists up to approximately $5h$ from each side. Consequently, it can be suspected that the effect of AR on the central flow starts to become negligible at some AR between 8 and 16, leading to the midspan flow behaving quasi-two-dimensionally. Given this, the proposed threshold (AR $\gtrsim$ 10) for minimal AR effect on flow behind a BFS with internal corners [32] and bluff bodies of finite length [39] may also be applicable to the present study.

D. Turbulence characteristics

Figure 10 presents the contours of the three components of Reynolds stresses, $\overline{u'u'}$, $\overline{w'w'}$, and $-\overline{u'w'}$, for all cases. For AR1, AR2, and AR16, the developments of Reynolds stresses are confined within a relatively narrow region below the step height. The contours for AR4 and AR8, however, spread out beyond the step height into a wider region, corresponding to the different mean flow structures observed in these cases (see Fig. 4). In the AR16 case, where the flow is nominally 2D, the distributions of all Reynolds stress components are relatively uniform along the streamwise direction, comparing well with the results behind a 2D BFS with AR of 62 [4]. Regardless of AR, the maximum values of the Reynolds stresses are concentrated around the mean reattachment location, followed by a rapid decay. The highest values for all three components are observed in the AR4 case, followed by the AR8 case, indicating more complex and turbulent flow behaviors in these cases.

To facilitate the investigation of the AR effect on Reynolds stresses, the streamwise variation of their maximum values is plotted in Fig. 11. Considering that X_r varies with AR, the streamwise distance is normalized by subtracting X_r and dividing by step height for a better comparison. A general pattern is observed, where the maximum value increases to a peak before the reattachment point and subsequently decreases, with the peaks of $\overline{w'w'}$ and $-\overline{u'w'}$ occurring closer to the reattachment point than that of $\overline{u'u'}$. The peak values increase from AR1 to AR4 and then reduce with larger AR. When AR = 16, the peak normalized values are 2.492×10^{-2}, 1.286×10^{-2}, and

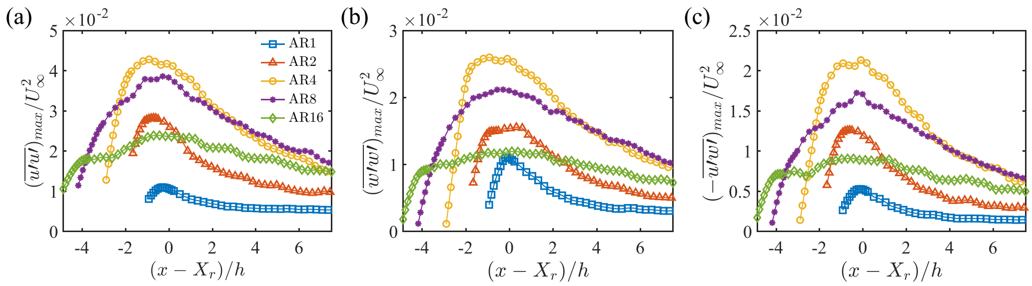

FIG. 11. Streamwise variation of the maximum Reynolds stresses (a) $\overline{u'u'}$, (b) $\overline{w'w'}$, and (c) $-\overline{u'w'}$.

0.997×10^{-2} for $\overline{u'u'}$, $\overline{w'w'}$, and $-\overline{u'w'}$, respectively, which match closely with the results in the 2D BFS study by Kostas *et al.* [4].

Nevertheless, it is known that the turbulence contains multiple scales of motion, and an object submerged in the turbulent flow would only experience the maximum loading from eddies of comparable size to it [46]. Therefore, it is necessary to consider the length scale of turbulence in addition to its intensity. The turbulence integral length scale is typically used to characterize the dimensions of eddies with high spectral energy [47]. The turbulence integral length scale (L_i, where $i = u$ or w) at a reference point ($x_{\text{ref}}, z_{\text{ref}}$) is evaluated as the square root of the integration of the two-point correlation (R_{ii}), as defined in Eqs. (1) and (2):

$$L_i(x_{\text{ref}}, z_{\text{ref}}) = \sqrt{\iint_{-\infty}^{\infty} R_{ii}\, dz\, dx}, \tag{1}$$

$$R_{ii}(x_{\text{ref}}, z_{\text{ref}}) = \frac{\overline{i'(x_{\text{ref}}, z_{\text{ref}})i'(x, z)}}{\sigma_i(x_{\text{ref}}, z_{\text{ref}})\sigma_i(x, z)}. \tag{2}$$

Here, i' denotes the instantaneous fluctuating component of velocity (u' or w'), and σ_i denotes the root mean square of the velocity fluctuation. Figure 12 presents the normalized streamwise and vertical turbulence integral length scale (L_u/h and L_w/h) behind the step. Based on the different color scales used, the values of L_w are apparently smaller than L_u while showing a similar variation with AR. The largest turbulence structures appear in the AR2 case, where the level of Reynolds stresses is moderate compared to the other cases (see Fig. 10). For AR4, despite possessing the highest turbulence intensity, the maximum streamwise scale of the eddies is the smallest among all cases, and the region containing relatively large-scale turbulence is much narrower. This implies that large-scale eddies may not contribute to intense fluctuations, highlighting the importance of considering turbulence length scale. Focused on the L_u maps, the largest structures are localized about $1h$ above the step height, extending from $2h$ to $6h$ downstream in all cases. For AR $\leqslant 4$, the wake region below the step height until the furthest reattachment location contains predominantly small-scale eddies. However, in cases with larger AR, very few small-scale eddies but eddies with comparable size to the step height appear in the central plane, indicating the transition from 3D to 2D flow.

E. Vortical structures

Within the separated shear layer, vortices form by rolling up due to Kelvin-Helmholtz instability and then grow by one or multiple amalgamations until they reattach to the bottom wall. After that, the vortices shed from the separation bubble and move downstream, while the reattached boundary layer recovers slowly. The evolution of those vortical structures within the free shear layer and the subsequent vortex shedding event directly contribute to intense turbulence and its rapid decay.

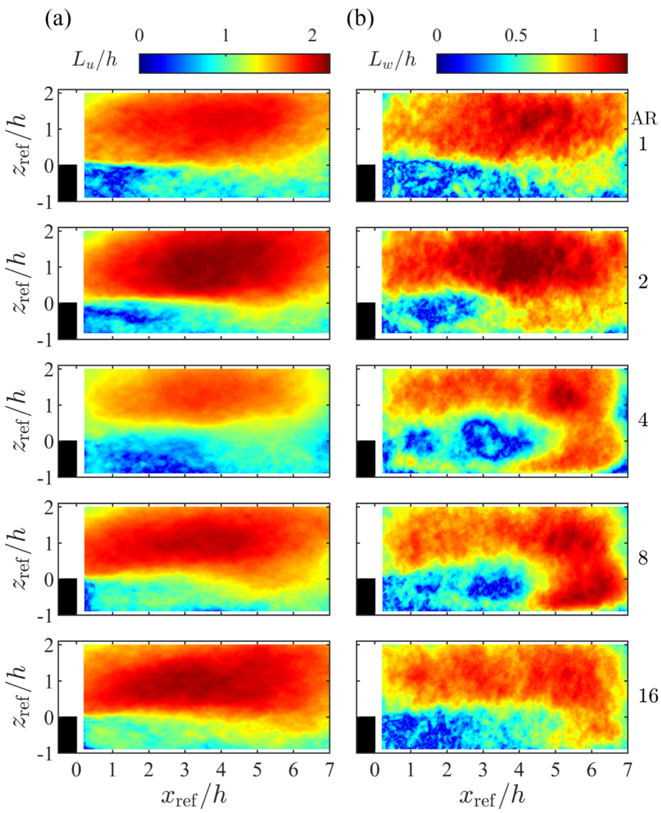

FIG. 12. Contours of (a) streamwise and (b) turbulence integral length scale (L_u and L_w).

Additionally, those induce the unsteady motion of the shear layer, as discussed in Sec. III C, and thus increase the complexity of the BFS flow.

The position-based vortical structures cannot be identified in the mean flow field but can be exhibited by the distribution of mean vorticity [4,13,17]. The out-of-plane (spanwise) mean vorticity (ω_y) is evaluated from the velocity gradients as

$$\omega_y = \frac{1}{2}\left(\frac{\partial U}{\partial z} - \frac{\partial W}{\partial x}\right). \tag{3}$$

Figure 13(a) shows the contours of normalized mean vorticity, $\omega_y h/U_\infty$, with contour levels of 3, 2, 1, 0.7, 0.5, 0.3, and 0. The positive vorticity indicates the region of clockwise-rotating vortices. The zero contour level is highlighted in red, separating regions with different vortical behavior. The thick blue dash-dotted line represents the dividing streamline ($\psi = 0$), which demonstrates the development direction of the vortical structures. The mean vorticity attains a peak value just behind the step edge within the separated shear layer and then decreases rapidly during the vortex pairing process, as indicated by the bulbous shape. A black dashed line is drawn connecting the downstream tips of contours, including those not displayed. The slightly upward-inclined bulbous shapes in the AR4 and AR8 cases consistently reflect the jettisoned flow pattern observed in Fig. 4.

The vorticity thickness (δ_{ω_y}) is also estimated by

$$\delta_{\omega_y} = \frac{U_{\max} - U_{\min}}{\left(\frac{\partial U}{\partial z}\right)_{\max}} \tag{4}$$

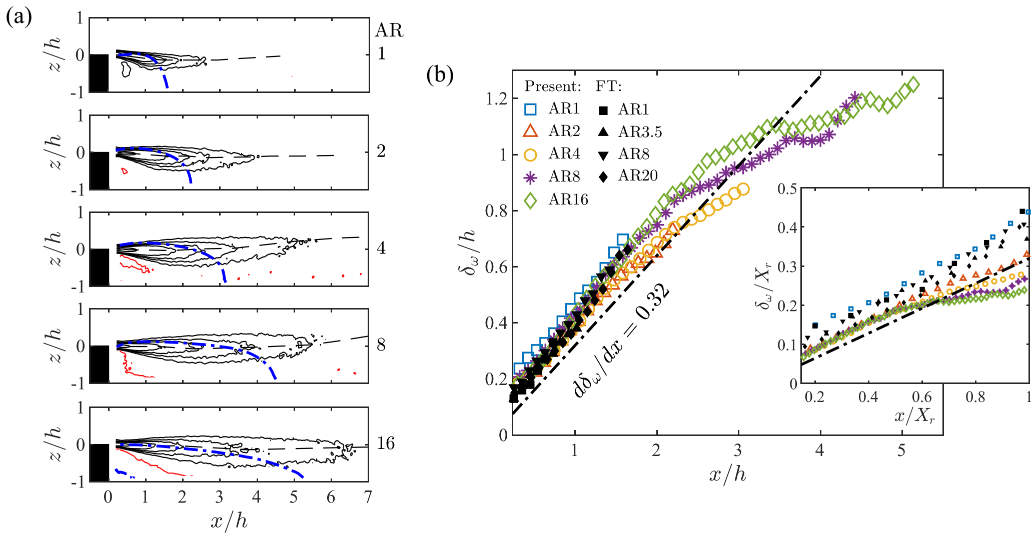

FIG. 13. (a) Contours of normalized mean vorticity ($\omega_y h/U_\infty$). The contour levels are 3, 2, 1, 0.7, 0.5, 0.3, and 0 (red). The blue dash-dotted line represents the diving streamline ($\psi = 0$), and the black dashed line connects downstream tips of contours. (b) Streamwise variation of vorticity thickness before the mean reattachment location, normalized by the step height (h) or mean reattachment length (X_r). The solid symbols plot the results over bluff bodies with finite streamwise length from Fang and Tachie [39].

to quantitatively study the development of the separated shear layer. As $(\partial U/\partial z)_{\max}$ is related to the shear layer, the vorticity thickness prior to the mean reattachment location is plotted in Fig. 13(b), and normalized by the mean reattachment length (X_r) in the inset. Within the upstream half of the shear layer, the vortical structures grow gradually along the streamwise direction in all cases, with a constant slope $d\delta_\omega/dx$ of 0.32. This slope is consistent with the finding by Fang and Tachie [39], who studied the separation bubble over bluff bodies with varying AR. Figure 13(b) also includes their data normalized by body height or mean reattachment lengths, which has a maximum of 1.6 body height. The variation of vorticity thickness in the present AR1 case ($X_r = 1.6h$) is comparable to their observations. Since our step height is only 2/3 of their body height, this may infer that the maximum scale of spanwise vortices within the shear layer is dependent on model height. However, this constant slope applies only to AR1 in the downstream half region. In all other cases, as the shear layer spreads further, its spreading becomes slower with increasing AR. This possibly implies that not only vortex amalgamation but also breakdown takes place, especially within a long separated and reattached shear layer.

IV. CONCLUSIONS

The flow over backward-facing steps (BFSs) with external corners and varying spanwise aspect ratios (AR) was investigated using the planar particle image velocimetry technique. Five models with a fixed streamwise length of 3.95 m, a fixed height of 19 mm, and AR (width/height) of 1, 2, 4, 8, and 16 were tested. The flow in the midspan behind the BFS is 3D for AR $\lesssim 4$, transitional when AR $= 8$, and nominally 2D when AR $= 16$. The flow in the AR16 case exhibits similar characteristics to the flow over a typical 2D BFS with internal corners which has been extensively studied in the literature. In addition, surface oil flow visualization was conducted to study the effect of AR on the flow behind the step. It is found that the 3D effect in the central flow can only be minimized when AR is larger than a value between 8 and 16, aligning with observations for flow over BFS with internal corners [32] and bluff bodies with short streamwise length [39], which require AR $\gtrsim 10$.

The wakes in the AR4 and AR8 cases display distinctly different flow patterns compared to the other cases, possibly due to the complex interaction between the separated flow and the corner vortices generated around the step side edges. It is speculated that the development of corner vortices is limited by the spanwise width of the step, with a dimension growing as AR increases and reaching a maximum at some AR between 4 and 8. After that, the corner vortices are separated, resulting in a diminished impact on the central flow. However, the corner vortices after separation are deflected subtly to the center [37], significantly affecting the wake in the AR8 case. Therefore, under the influence of relatively large-scale corner vortices that are in close proximity, as well as possibly from sidewall shear layers, a jettisoned flow away from the bottom wall is observed in the wakes when AR = 4 and 8. The elevation of the mean separation bubble core in the AR1 and AR2 cases reveals a transition to flow ejection. Such an upwash effect is also reflected in the distributions of Reynolds stresses and mean vorticity.

The mean reattachment length increases monotonically with small AR and then tends to approach a constant level, as observed behind bluff bodies [38,39]. However, this increase with AR is contrary to the observation behind BFS with internal corners [32], likely attributed to the difference in secondary flow behavior between internal and external corner regions. In addition, due to the flapping motion of the shear layer, the instantaneous reattachment point oscillates within a zone. The shortest reattachment length stabilizes when AR = 8, while the longest reattachment length keeps increasing with AR and is expected to reach an asymptotic value when AR $\geqslant$ 16.

An analysis of turbulence characteristics is performed. The level of Reynolds stresses increases monotonically with AR from 1 to 4, followed by a decrease with larger AR. Corresponding to the distinct flow structures observed, the distributions of all three components of Reynolds stresses in the AR4 and AR8 cases spread into a wider region beyond the step height, while those in the other cases are confined within a relatively narrow region below the step height. However, unlike the peak values of Reynolds stresses, the turbulence integral length scale is the largest in the AR2 case and the smallest for AR4. This indicates that an object with a relatively large size would experience greater loading from turbulence when positioned behind a step with AR of 2.

Furthermore, the mean spanwise vorticity consistently demonstrates the AR effect on the development of vortical structures within the separated shear layer. The shear layer spreads at a constant rate in the first half region, while the growth of vortices in the second half region slows down further as AR gets larger. This implies that the vortical structures have a limited scale and they may not only grow by pairing but also break down into smaller scales, especially within a long separated and reattached shear layer.

At this point, it is also worth mentioning some limitations of this study and prospective future work. The results presented in this study may have been influenced by the spatial resolution of the PIV system. Insufficient resolution of smaller-scale turbulence structures could potentially lead to an underestimation of Reynolds stresses, integral length scales, and vorticity. Moreover, PIV measurements in a single plane limit our ability to fully capture the 3D wake behaviors, particularly regarding the development of corner vortices and their interaction with the separated flow. Due to constraints in resources and time, we were unable to conduct follow-up investigations. To gain deeper insights into the dynamics of the step wake, especially for AR4 and AR8, future studies could employ the PIV technique in multiple planes or utilize numerical simulations to provide a comprehensive 3D view of the flow structure. It might also be worthwhile to track the development of eddies using time-resolved methods, as transient flow features could reveal valuable details on the evolution of vortical structures.

While this study focuses on simple step models, future research could explore more intricate geometries, such as ship superstructures, and investigate the effects of corner modifications, such as round corners. These efforts would provide deeper insights into how various structural features affect wake behavior, which could be beneficial for optimizing aerodynamic designs and turbulent wake features for ships, buildings, trains, and other engineering applications involving steplike structures.

[1] L. Chen, K. Asai, T. Nonomura, G. Xi, and T. Liu, A review of backward-facing step (BFS) flow mechanisms, heat transfer and control, Therm. Sci. Eng. Prog. **6**, 194 (2018).

[2] F. W. Roos and J. T. Kegelman, Control of coherent structures in reattaching laminar and turbulent shear layers, AIAA J. **24**, 1956 (1986).

[3] J. Kim, S. J. Kline, and J. P. Johnston, Investigation of a reattaching turbulent shear layer: Flow over a backward-facing step, ASME J. Fluids Eng. **102**, 302 (1980).

[4] J. Kostas, J. Soria, and M. Chong, Particle image velocimetry measurements of a backward-facing step flow, Exp. Fluids **33**, 838 (2002).

[5] F.-F. Wang, S.-Q. Wu, and B. Huang, Flow structure and unsteady fluctuation with separation over a two-dimensional backward-facing step, J. Hydrodyn. **31**, 1204 (2019).

[6] L. M. Hudy, A. Naguib, and W. M. Humphreys, Stochastic estimation of a separated-flow field using wall-pressure-array measurements, Phys. Fluids **19**, 024103 (2007).

[7] J. Rajasekaran, On the flow characteristics behind a backward-facing step and the design of a new axisymmetric model for their study, Master's thesis, University of Toronto, 2011.

[8] K. A. M. Moinuddin, P. N. Joubert, and M. S. Chong, Experimental investigation of turbulence-driven secondary motion over a streamwise external corner, J. Fluid Mech. **511**, 1 (2004).

[9] D. E. Abbott and S. J. Kline, Experimental investigation of subsonic turbulent flow over single and double backward-facing steps, ASME J. Basic Eng. **84**, 317 (1962).

[10] P. Bradshaw and F. Y. F. Wong, The reattachment and relaxation of a turbulent shear layer, J. Fluid Mech. **52**, 113 (1972).

[11] F. Durst and C. Tropea, Flows over two-dimensional backward-facing steps, in *Proceedings of Structure of Complex Turbulent Shear Flow IUTAM Symposium*, edited by R. Dumas and L. Fulachier (Springer-Verlag, Marseille, France, 1982), pp. 41–52.

[12] P. M. Nadge and R. N. Govardhan, High Reynolds number flow over a backward-facing step: Structure of the mean separation bubble, Exp. Fluids **55**, 1657 (2014).

[13] F.-F. Wang, A. Gao, S.-Q. Wu, S.-L. Zhu, J.-Y. Dai, and Q. Liao, Experimental investigation of coherent vortex structures in a backward-facing step flow, Water **11**, 2629 (2019).

[14] H. Le, P. Moin, and J. Kim, Direct numerical simulation of turbulent flow over a backward-facing step, J. Fluid Mech. **330**, 349 (1997).

[15] M. Barri, G. K. E. Khoury, H. I. Andersson, and B. Pettersen, DNS of backward-facing step flow with fully turbulent inflow, Int. J. Numer. Methods Fluids **64**, 777 (2010).

[16] J. L. Aider, A. Danet, and M. Lesieur, Large-eddy simulation applied to study the influence of upstream conditions on the time-dependant and averaged characteristics of a backward-facing step flow, J. Turbul. **8**, N51 (2007).

[17] R. Hu, L. Wang, and S. Fu, Investigation of the coherent structures in flow behind a backward-facing step, Intl J. Numer. Methods Heat Fluid Flow **26**, 1050 (2016).

[18] J. K. Eaton and J. P. Johnston, A review of research on subsonic turbulent flow reattachment, AIAA J. **19**, 1093 (1981).

[19] R. Y. Hu, L. Wang, and S. Fu, Review of backward-facing step flow and separation reduction (in Chinese), Sci. Sin.-Phys. Mech. Astron. **45**, 124704 (2015).

[20] F. Scarano and M. L. Reithmuller, Iterative multigrid approach in PIV image processing with discrete window offset, Exp. Fluids **26**, 513 (1999).

[21] P. Spazzini, G. Iuso, M. Onorato, N. Zurlo, and G. M. D. Cicca, Unsteady behavior of back-facing step flow, Exp. Fluids **30**, 551 (2001).

[22] S. D. Hall, M. Behnia, C. A. J. Fletcher, and G. L. Morrison, Investigation of the secondary corner vortex in a benchmark turbulent backward-facing step using cross-correlation particle imaging velocimetry, Exp. Fluids **35**, 139 (2003).

[23] C. Shih and C. M. Ho, Three-dimensional recirculation flow in a backward facing step, ASME J. Fluids Mech. **116**, 228 (1994).

[24] T. R. Troutt, B. Scheelke, and T. R. Norman, Organized structures in a reattaching separated flow field, J. Fluid Mech. **143**, 413 (1984).

[25] G. L. Brown and A. Roshko, On density effects and large structure in turbulent mixing layers, J. Fluid Mech. **64**, 775 (1974).
[26] C. D. Winant and F. K. Browand, Vortex pairing: The mechanism of turbulent mixing-layer growth at moderate Reynolds number, J. Fluid Mech. **63**, 237 (1974).
[27] Y. Z. Liu, W. Kang, and H. J. Sung, Assessment of the organization of a turbulent separated and reattaching flow by measuring wall pressure fluctuations, Exp. Fluids **38**, 485 (2005).
[28] D. M. Driver, H. L. Seegmiller, and J. G. Marvin, Time-dependent behavior of a reattaching shear layer, AIAA J. **25**, 914 (1987).
[29] R. L. Simpson, Review—a review of some phenomena in turbulent flow separation, ASME J. Fluids Eng. **103**, 520 (1981).
[30] B. F. Armaly, F. Durst, J. C. F. Pereira, and B. Schönung, Experimental and theoretical investigation of backward-facing step flow, J. Fluid Mech. **127**, 473 (1983).
[31] E. W. Adams and J. P. Johnston, Effects of the separating shear layer on the reattachment flow structure part 2: Reattachment length and wall shear stress, Exp. Fluids **6**, 493 (1988).
[32] V. de Brederode and P. Bradshaw, Three-dimensional flow in nominally two-dimensional separation bubbles. I. Flow behind a rearward-facing step, Technical Report No. 72-19 (Imperial College of Science and Technology, 1972).
[33] K. Chauhan, J. Philip, C. M. de Silva, N. Hutchins, and I. Marusic, The turbulent/non-turbulent interface and entrainment in a boundary layer, J. Fluid Mech. **742**, 119 (2014).
[34] Kevin, J. Monty, and N. Hutchins, Turbulent structures in a statistically three-dimensional boundary layer, J. Fluid Mech. **859**, 543 (2019).
[35] R. J. Adrian and J. Westerweel, *Particle Image Velocimetry* (Cambridge University Press, Cambridge, UK, 2011).
[36] F. K. Lu, Surface oil flow visualization, Eur. Phys. J. Spec. Top. **182**, 51 (2010).
[37] C. E. Tinney and L. S. Ukeiley, A study of a 3-D double backward-facing step, Exp. Fluids **47**, 427 (2009).
[38] R. Martinuzzi and C. Tropea, The flow around surface-mounted, prismatic obstacles placed in a fully developed channel flow (data bank contribution), ASME J. Fluids Eng. **115**, 85 (1993).
[39] X. Fang and M. F. Tachie, Flows over surface-mounted bluff bodies with different spanwise widths submerged in a deep turbulent boundary layer, J. Fluid Mech. **877**, 717 (2019).
[40] K. C. Kim, H. S. Ji, and S. H. Seong, Flow structure around a 3-D rectangular prism in a turbulent boundary layer, J. Wind. Eng. Ind. Aerodyn. **91**, 653 (2003).
[41] G. Eitel-Amor, R. Örlü, and P. Schlatter, Simulation and validation of a spatially evolving turbulent boundary layer up to $Re_\theta = 8300$, Int. J. Heat Fluid Flow **47**, 57 (2014).
[42] J. H. Lee, Kevin, J. P. Monty, and N. Hutchins, Validating under-resolved turbulence intensities for PIV experiments in canonical wall-bounded turbulence, Exp. Fluids **57**, 129 (2016).
[43] N. Kasagi and A. Matsunaga, Three-dimensional particle-tracking velocimetry measurement of turbulence statistics and energy budget in a backward-facing step flow, Int. J. Heat Fluid Flow **16**, 477 (1995).
[44] S. Chun, Y. Z. Liu, and H. J. Sung, Wall pressure fluctuations of a turbulent separated and reattaching flow affected by an unsteady wake, Exp. Fluids **37**, 531 (2004).
[45] H. Xu and A. Pollard, Large eddy simulation of turbulent flow in a square annular duct, Phys. Fluid **13**, 3321 (2001).
[46] P. Mendis, T. Ngo, N. Haritos, A. Hira, B. Samali, and J. Cheung, Wind loading on tall buildings, Elec. J. Struct. Eng. **7**, 41 (2007).
[47] M. J. Emes, M. Arjomandi, F. Ghanadi, and R. M. Kelso, Effect of turbulence characteristics in the atmospheric surface layer on the peak wind loads on heliostats in stow position, Solar Energy **157**, 284 (2017).